AIP Advances

Biomedical device prototype based on small scale hydrodynamic cavitation

Cite as: AIP Advances **8**, 035108 (2018); https://doi.org/10.1063/1.5005048
Submitted: 16 September 2017 . Accepted: 26 February 2018 . Published Online: 08 March 2018

Morteza Ghorbani, Canberk Sozer, Gokhan Alcan, Mustafa Unel, Sinan Ekici, Huseyin Uvet, and Ali Koşar

View Online Export Citation CrossMark

ARTICLES YOU MAY BE INTERESTED IN

Intensifying cavitating flows in microfluidic devices with poly(vinyl alcohol) (PVA) microbubbles
Physics of Fluids **30**, 102001 (2018); https://doi.org/10.1063/1.5051606

Enhancing the aggressive intensity of hydrodynamic cavitation through a Venturi tube by increasing the pressure in the region where the bubbles collapse
AIP Advances **6**, 045113 (2016); https://doi.org/10.1063/1.4947572

Energy harvesting with micro scale hydrodynamic cavitation-thermoelectric generation coupling
AIP Advances **9**, 105012 (2019); https://doi.org/10.1063/1.5115336

NEW
AVS Quantum Science
A new interdisciplinary home for impactful quantum science research and reviews
NOW ONLINE
Co-Published by
AIP Publishing AVS

AIP Publishing

© 2018 Author(s).

Biomedical device prototype based on small scale hydrodynamic cavitation

Morteza Ghorbani,[1,2] Canberk Sozer,[3] Gokhan Alcan,[2,4] Mustafa Unel,[2,4] Sinan Ekici,[5] Huseyin Uvet,[3] and Ali Koşar[2,6,a]

[1]*Sabancı University Nanotechnology Research and Applications Center, Orta Mahalle, 34956 Tuzla, Istanbul, Turkey*
[2]*Mechatronics Engineering Program, Faculty of Engineering and Natural Science, Sabancı University, Orhanli-Tuzla, Istanbul 34956, Turkey*
[3]*Mechatronics Engineering Department, Yildiz Technical University, Istanbul 34956, Turkey*
[4]*Integrated Manufacturing Technologies Research and Application Center, Sabanci University, Tuzla, Istanbul 34956, Turkey*
[5]*Department of Urology, Hisar Intercontinental Hospital, Istanbul 34750, Turkey*
[6]*Center of Excellence for Functional Surfaces and Interfaces for Nano-Diagnostics (EFSUN), Sabancı University, Orhanli-Tuzla, Istanbul 34956, Turkey*

(Received 16 September 2017; accepted 26 February 2018; published online 8 March 2018)

This study presents a biomedical device prototype based on small scale hydrodynamic cavitation. The application of small scale hydrodynamic cavitation and its integration to a biomedical device prototype is offered as an important alternative to other techniques, such as ultrasound therapy, and thus constitutes a local, cheap, and energy-efficient solution, for urinary stone therapy and abnormal tissue ablation (e.g., benign prostate hyperplasia (BPH)). The destructive nature of bubbly, cavitating, flows was exploited, and the potential of the prototype was assessed and characterized. Bubbles generated in a small flow restrictive element (micro-orifice) based on hydrodynamic cavitation were utilized for this purpose. The small bubbly, cavitating, flow generator (micro-orifice) was fitted to a small flexible probe, which was actuated with a micromanipulator using fine control. This probe also houses an imaging device for visualization so that the emerging cavitating flow could be locally targeted to the desired spot. In this study, the feasibility of this alternative treatment method and its integration to a device prototype were successfully accomplished. © *2018 Author(s). All article content, except where otherwise noted, is licensed under a Creative Commons Attribution (CC BY) license (http://creativecommons.org/licenses/by/4.0/).*
https://doi.org/10.1063/1.5005048

INTRODUCTION

Ultrasonic cavitation for the treatment of urinary stones is well known under the scheme of shock wave lithotripsy (SWL). This technique has been the standard method of lithotripsy for many years, with a fragmentation rate of 97%.[1] The main part of SWL is a lithotripter that uses electrohydraulic, ultrasound, or laser energy.[2] While it is proven that the wave exposure during SWL damages healthy cells around the kidney stone,[3–6] recent investigations have shown that the modern lithotripters are highly ineffective and may cause severe injuries in comparison to traditional lithotripters.[7] Moreover, the applicability of these devices is not universally successful, especially in the setting of hard stones, such as those consisting of calcium oxalate monohydrates and calcium phosphate cysteines. Another disadvantage is the potential of overheating due to the conversion of vibration energy to heat energy.[8]

Intracorporal lithotripsy is the key step affecting the success rate of endoscopic surgery for urinary stones. In this step, pneumatic, ultrasonic, and laser lithotripters, are commonly used as energy sources.[9] Pneumatic lithotripters work based on the same principle as that in the case of a

[a]Corresponding Author: kosara@sabanciuniv.edu

 © Author(s) 2018

collision with a bullet. They are based on an impact upon which energy is transmitted via compressed air pulses propagating within a steel probe to fragment the calculi.[10] This technique offers safe, cheap, and effective clearance of calculi. It is also particularly useful for large and hard stones. Moreover, all the stones can be destroyed regardless of their composition, but subsequent extraction of the stone fragments is required.[11,12] The application of laser is one of the intracorporal lithotripsy methods. In spite of the advantages of this method, laser energy might cause urethral wall injury owing to its increased power.[13]

The lithotripter's energy is exploited via different surgical treatment methods for urinary stones. Percutaneous nephrolithotomy (PCNL)[14] is a minimally invasive surgical method where the physician directly intervenes to dissect large kidney stones from the kidney through the skin. Retrograde intrarenal surgery (RIRS)[15] is a minimally invasive method where the device enters the body through the urethra and reaches the kidneys via the ureter. Cystoscopy[16] is another minimally invasive method which is used for bladder stones.

New, alternative, methods are sought to reduce the side effects and increase the efficiency in the treatment of urinary stones. Hydrodynamic cavitation is considered as a strong alternative in urinary stone treatment. Hydrodynamic cavitation is generated by the reduction in static pressure of the liquid below a critical level due to a sudden flow restriction. It leads to the generation of cavitation bubbles (inception) and cavitating flows. Two regions are apparent inside the flow restrictive element: recirculation zones and vena contracta. Recirculation zones generated in the vicinity of the walls, where cavitation bubbles appear. These zones may be moved towards the end of the restriction depending upon the pressure difference. Vena contracta is located between two recirculation zones and includes high speed liquid jet restricted by cavitation bubbles. The vena contracta is generated at the entrance of the restrictive element, and the flow restrictive element may be filled with cavitation bubbles downstream of its entrance at high pressures particularly in micro scale hydrodynamic cavitation.[17,18] Cavitation is a dynamic phenomenon and includes successive growth of bubbles and their lateral rupture. While the low static pressure induced by the flow restrictive element is the reason for the formation of cavitation bubbles in hydrodynamic cavitation, an acoustic field with a sufficient intensity results in pressure oscillations in the ultrasound cavitation, leading to emergence of bubbles.

Shock wave lithotripsy (SWL) as an ultrasound-based noninvasive method benefits from two effective mechanisms for kidney stone fragmentation: shock wave effects and cavitation phenomenon. It was reported that the erosion on kidney stones exposed to SWL was achieved due to the direct impact of created shock waves.[19] In contrast to hydrodynamic cavitation, where a flow restrictive element causes a pressure drop, there is a need for a shock wave generator, a focusing device and a system for handling the target in the SWL treatment to induce the pressure. While the flow restriction geometry and surface topology are considered as the key parameters in hydrodynamic cavitation, parameters involving acoustics in lithotripsy determine the morphology of cavitation bubbles in the SWL. Therefore, the formation and collapse of the bubbles are in a close relation for hydrodynamic cavitation and SWL.[20]

The emerging bubbles have a small size, high energy, and may become destructive. They can be utilized with the support of an endoscopic device for the fragmentation of stones. The endoscopes are used for both the visualization and intervention of the body. The endoscope, which is used for endoscopic examinations and interventions of the urethra and urinary bladder, is called cystoscope. A cystoscope is inserted in the body through the urethra, and allows surgeons to conduct operations in the bladder for several pathologies, in both male and female patients. It is attached to a camera with an illumination source for imaging. The camera transmits the real-time images from the region of operation to the operator. Cystoscopes can be grouped as rigid and flexible ones. The rigid cystoscopes consist of a rigid tube. To steer the rigid cystoscopes, the entire device must be repositioned towards the target. The flexible cystoscopes have a flexible section in addition to the rigid tube so that the operator can control the flexible section of the device using a joystick. The flexible part of a cystoscope can be steered using different actuation methods, such as the tendon driven, shape memory alloy (SMA), and concentric tube or fluid.[21–23]

In this study, a flexible cystoscope prototype is developed for use in the fragmentation of urinary stones based on hydrodynamic cavitation. The tendon-driven prototype is controlled via a manual

joystick. The prototype guides the generated cavitation bubbles in the cavitation tube (microprobe) towards the stone. The prototype is actuated by a Stewart platform. The motions of the platform around the X- and/or the Y-axes are transmitted to the flexible end effector arms through four 90° circularly positioned stainless steel tendon wires. These wires generate two antagonistic tendon pairs. When the Stewart platform bends by at most ±4° around the X- and/or Y-axes, the flexible end effector arms bend by at most ±40° in the X- and/or Y-axes. Therefore, real time visual feedback from the camera is obtained while the joystick commands are processed. The prescribed system achieves excellent operational conditions to guide the cavitation probe to the targeted area.

THE PROPOSED PROTOTYPE UTILIZING HYDRODYNAMIC CAVITATION

The prototype, shown in Figure 1, includes three main parts, namely, the hydrodynamic cavitation section, a flexible micromanipulator, and an imaging system. The cavitation bubbles are generated inside the microchannel owing to a sudden flow restriction. The microchannel is connected to the stainless-steel tube (inner diameter of 4.5 mm) with appropriate fittings. A high-pressure nitrogen tank is utilized to provide the required injection pressure for the fluid deposited in the liquid container. Pressure gauges, control valves, and a microfilter, are mounted on the tube to measure and control the fluid flow. The microchannel, which is made of stainless steel, is 15 cm long and has an outer diameter of 1 mm, while its nominal inner diameter is reduced from 900 μm to 100 μm in part of its length, along a distance of 14.6 cm.

The developed flexible micromanipulator contains two channels, one for the microchannel, and another for the waterproof medical nested imaging and illuminating system. Thanks to the medical camera inside the flexible prototype, the operator receives real time visual feedback, and repositions the joystick to reach the target. The probe has a 10 mm in outer diameter, and the flexible end effector arms can bend by at most 40° along the ±X and ±Y axes through the use of the micromanipulator. The prototype parts were designed in the 3D CAD (Computer Aided Design) software SolidWorks, and manufactured by an EOS M290 DMLS 3D printer. The produced parts were assembled with stainless-steel tendon wires, and actuated by a Newport HXP50 – MECA 6 axis hexapod. The control of the hexapod was achieved by the Newport HXP50 – ELEC controller via MATLAB.

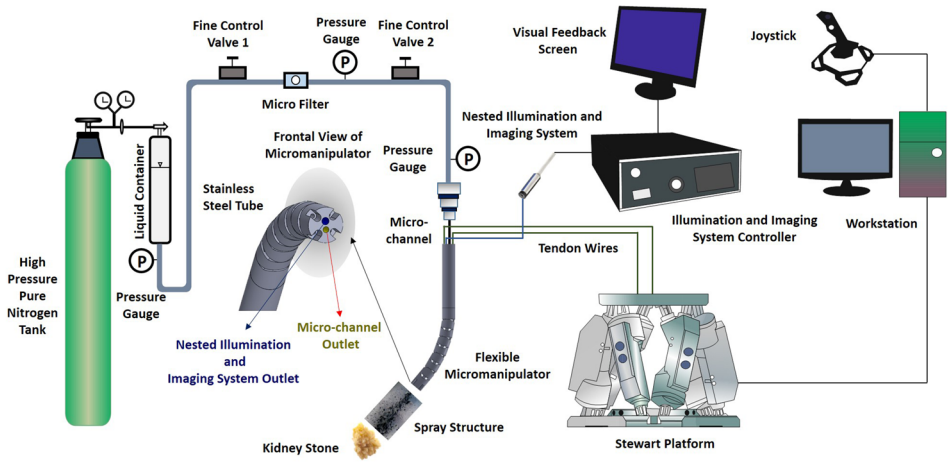


FIG. 1. Experimental setup that includes the hydrodynamic cavitation section, control, and imaging system. Shown also, is the flexible micromanipulator used to control the cavitation probe and imaging system. A high-pressure tank containing pure Nitrogen (Linde Gas, Gebze, Kocaeli) supplies the required upstream pressure for the system. This tank is connected to a fluid reservoir (Swagelok, Erbusco BS, Italy), which is filled with Phosphate buffered saline (PBS) and serves as the working fluid. The reservoir is connected to the system with adaptor fittings. Three pressure sensors (Omega, USA) are mounted at the initial, middle-, and end-parts of the tubing system to measure the pressures. Two fine control valves (Swagelok) are integrated in the system to control the flow at the desired locations. A micro T-type filter (Swagelok) with a nominal pore size of 15 μm is used to filter particles larger than 15 μm. The Stewart platform is used to control the flexible micromanipulator, which was manufactured by an EOS M290 DMLS 3D printer, and a medical camera (Medigus Ltd, Israel) was utilized to track the formed spray on the targeted areas (kidney stone, prostate tissue, etc).

The flexible cystoscope system is designed and manufactured to guide the bubbles which are generated by hydrodynamic cavitation inside the stainless steel microchannel, and directed to the urinary stone specimen, as shown in Figure 2. The system includes a tendon-driven prototype, which has a flexible section for bending—achieving angles up to ±40° along the X- and the Y-axes—a joystick to control the flexible section, a Stewart platform as a manipulator, a waterproof medical camera enclosed by the fiber optic illumination system to provide visual feedback to the operator, and a hydrodynamic cavitation probe to generate cavitation bubbles. The flexible section of the prototype is controlled by a manual joystick. The operator receives continuous visual feedback from the imaging system and gives appropriate inputs to the Stewart platform through the joystick. The joystick inputs are processed by MATLAB, and appropriate roll-and-pitch motion commands are generated for the Stewart platform. Roll-and-pitch motions realized by the Stewart platform are transmitted to the flexible section of the prototype via stainless-steel tendon wires. The flexible cystoscope prototype was designed and implemented to have improved features that would lead to advantages in patient recovery over the rigid cystoscope, such as the shorter hospitalization times, fewer post-operative symptoms, and increased patient and physician comfort.[24–26]

The prototype is able to locally target the urinary stone to treat the well defined edges of the urinary stone in the bladder. During interventional urinary stone operations, there is urine in the bladder. Owing to the pressure of the water jet, the urinary stone moves freely inside the urine-filled bladder when the cavitating flow is exposed. For this reason, the flexibility of the arms is important for tracking the stone. The prototype has six channels: a 1.7 mm diameter channel for a 1.6 mm outside diameter hydrodynamic cavitation probe, a 2.1 mm diameter channel for a 2 mm diameter imaging system, and four 90° circularly positioned 1.25 mm diameter channels for 1 mm stainless-steel tendon wires. The flexible section is able to bend owing to the teeth–hole structure. When these factors are taken into consideration, the total outer diameter of the prototype becomes 10 mm. The flexibility is provided by the assembly of the four different micromanipulator spacers in a proper order, which include the base part, bendable spacer along the X-axis, bendable spacer along the Y-axis, and a distal end-part. The base part has teeth on the top surface, the distal end-part has holes on the bottom surface, the X- and Y- bendable spacers have teeth on the top surfaces and holes

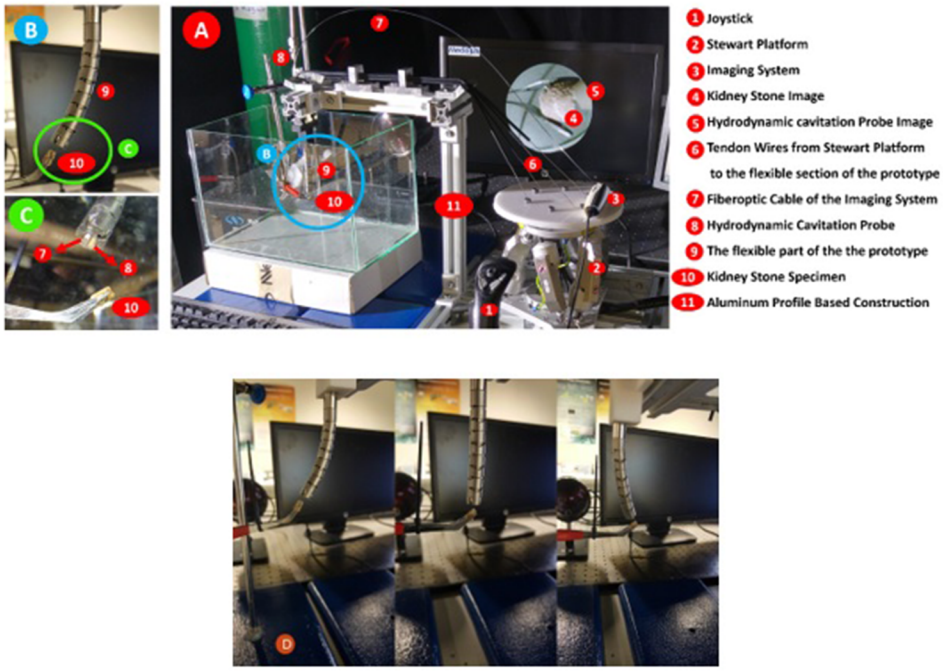


FIG. 2. (A) The setup of the whole system. (B) The flexible section of the system used for urinary stone-specimen interactions, and (C) the components of the prototype. (D) Indicative photographs showing the bending of the micromanipulator.

on the bottom surfaces. Owing to the teeth-hole structure of the micromanipulator spacers, centering and bending of the flexible section is possible. The flexible section consists of nine micromanipulator spacers because the bendable spacers along the X- and Y-axes are used three and four times each, respectively. This alignment creates eight joint points, and bending occurs at these points. Four of these joints provide bending along the X-axis, while the remaining joints allow bending along the Y-axis. Each joint bends up to ±10° along a single axis, and thus, the total flexible section is able to bend up to ±40° along the X- and Y-axes.

ACTUATION AND CONTROL OF THE PROTOTYPE

The Stewart platform has been chosen as an actuator to steer the flexible section of the cystoscope prototype owing to its motion capabilities. The platform is able to move translationally and rotationally along the X, Y, and Z axes. To control the flexible section, rotational motion capabilities around the X- (roll) and Y- (pitch) axes have been used. The motions of the Stewart platform are transmitted to the flexible section via four stainless steel tendon wires. The tips of the four tendons are fixed to the distal-end part, and other tips are attached over the Stewart platform passing through all micromanipulator spacers. The 90° circularly positioned tendon wires move antagonistically. When a single tendon is pulled to a certain extent, the cross-tendon is released in the opposite direction. To control the flexible prototype along a single axis, two antagonistic tendon pairs must be controlled simultaneously. The mechanical structure of the Stewart platform allows the control of the tendon pairs easier than controlling the tendons individually using more than one motor. For this reason, the Stewart platform is highly suitable for controlling the flexible prototype.

To control the prototype, the relationship between the device space (the Stewart platform) and the task space has been modeled (Figure 3). The relationship between the task space (x, y, and z) and the configuration space (θ and ϕ) is expressed by equation (1).[27] Accordingly, the desired positions of the distal-end (x, y, z) are provided as the input to the system by the operator through the joystick.

$$\begin{bmatrix} \theta \\ \phi \end{bmatrix} = \begin{bmatrix} \frac{2N-1}{N} arctan\left(\frac{\sqrt{x^2+y^2}}{z}\right) \\ arctan\left(\frac{y}{x}\right) \end{bmatrix} \tag{1}$$

where N is the total number of joints, (x, y, z) are the spatial coordinates of the distal-end, θ is the bending angle, and ϕ is the direction angle. The relationship between the configuration space (θ and ϕ), and the actuator space (L_1, L_2, L_3, and L_4) is expressed by equation (2).[28] This equation is used to identify the required linear displacement of the tendon wires (L_1, L_2, L_3, and L_4) from the calculated angles θ and ϕ (1) as follows:

$$L_i = L_0 + 2N_f \left[\alpha_i sin\left(\frac{\theta}{2}\right) + \beta_i sin^2\left(\frac{\theta}{4}\right)\right], \quad i = 1, 2, 3, 4 \tag{2}$$

where $\alpha_1 = -\alpha_3 = \frac{d}{2}\cos(\phi)$, $\alpha_2 = -\alpha_4 = \frac{d}{2}\sin(\phi)$, $\beta_1 = \beta_2 = \beta_3 = \beta_4 = -h_0$. In these expressions, L_0 is the length of tendons at the initial position, N_f is the free-joint number, d is the pairwise distance between tendons, ϕ is the bending direction, α_1 and α_2 are the distances of the tendons to the bending neutral plane, θ is the total bending angle, and h_0 is the joint gap distance. Finally, the relationship between the actuator space (L_1, L_2, L_3 and L_4) and the device space is expressed as,

$$\{L_i\} = c\ tan\ (\gamma) \tag{3}$$

where c is a constant value, γ is the bending angle of the Stewart platform, and $\{L_i\}$ denotes the coordinates (L_1, L_2, L_3, and L_4). A uniformly perforated Plexiglas plate is attached on the top surface of the Stewart platform. The tendon wires are fixed to holes in the plate. In this case, c is the horizontal distance of a chosen hole from the origin of the coordinate system. When the Stewart platform bends by 4° around the X-axis (roll) or the Y-axis (pitch), two of the four tendon wires are pulled by 2.5 mm, and the other two tendons are released by the same amount. The bending mechanism is controlled by a manual joystick. The joystick commands have been processed by MATLAB, and motion commands are generated for the Stewart platform. According to the commands, the platform bends around the X- and/or Y-axes, and bending occurs at the flexible section of the arms.

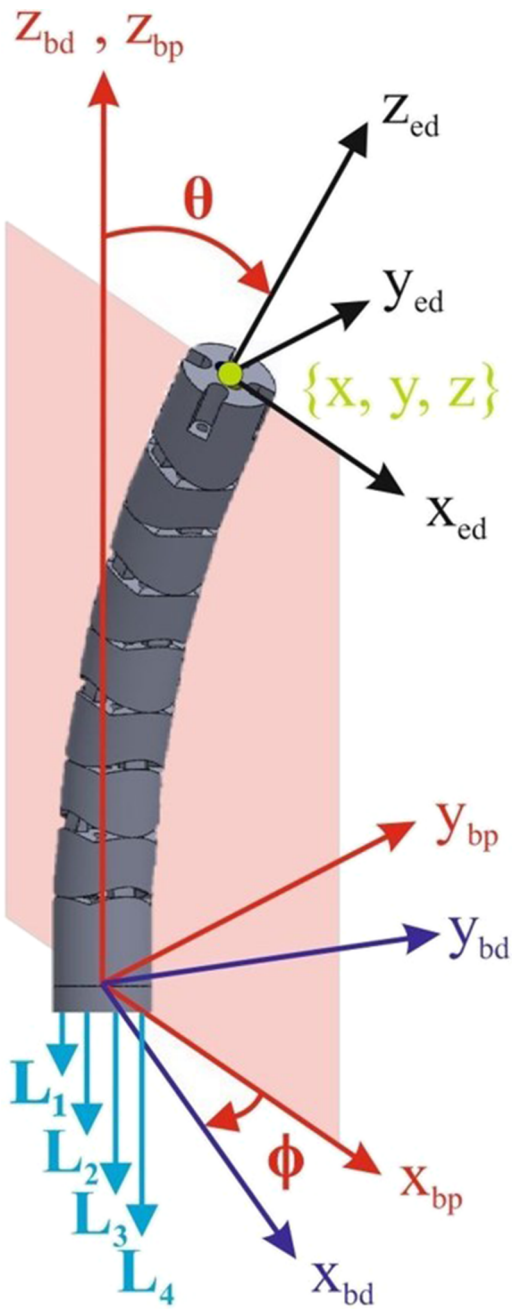


FIG. 3. Coordinate systems used to define the bending motion. $\{L_1, L_2, L_3, L_4\}$ are tendon lengths, $\{x_{bd}, y_{bd}, z_{bd}\}$ denote the coordinate system for the base disk, $\{x_{bp}, y_{bp}, z_{bp}\}$ denote the coordinate system for the bending plane, and $\{x_{ed}, y_{ed}, z_{ed}\}$ denote the coordinate system for the end-disk.

VISUALIZATION OF CAVITATING FLOWS

We have employed the particle shadow sizing (PSS)[29] technique to monitor the cavitating flow, and have developed novel vision-based algorithms to extract some visual information and estimate important parameters related to the hydrodynamic cavitation phenomenon. Briefly, PSS is a whole-field imaging technique, where noncoherent power LEDs or single/dual high power lasers are located on the optical axis of a high-speed camera so that the particles, such as bubbles, droplets, and small solid structures—e.g., powder—can be visualized as shadows at the micron scale, with the use of appropriate magnification levels. Since the PSS technique does not depend

on the scattering light from the surface of the observed particles thanks to direct in-line illumination, these particles do not need to be shiny or spherical as in the cases of LDA,[30] PDA,[31] or IPI.[32] The employed visualization system provides frame rates up to 10 kHz, and an image resolution of 1600×1200 pixels^2 for an 857 x 610 μm^2 area.

In order to enhance the acquired microscopic shadow images, several preprocessing operations[33] are employed, such as noise removal, adaptive contrast stretching, morphological operations, and connected component analysis. Scattered bubbles around the main jet flow are modeled and analyzed in accordance to the Gaussian distribution.[34] The cone angle of the jet flow is estimated with a Kalman-filter-based technique for different inlet pressures ranging from 10 to 120 bar.[35] A novel tracking algorithm is developed to track individually segmented single, double, and triple droplets, within jet flows.[36] The contours of the tracked droplets are then modeled using elliptical Fourier descriptors, and the extracted unique parameters are investigated to analyze their evolution in time.

RESULTS

Exposure of cavitating flows to urinary stones

A shadow strobe apparatus and a dual-pulse laser source that make the laser beam a homogenous light source, were used as the illumination source. The enlargement ratio was increased from

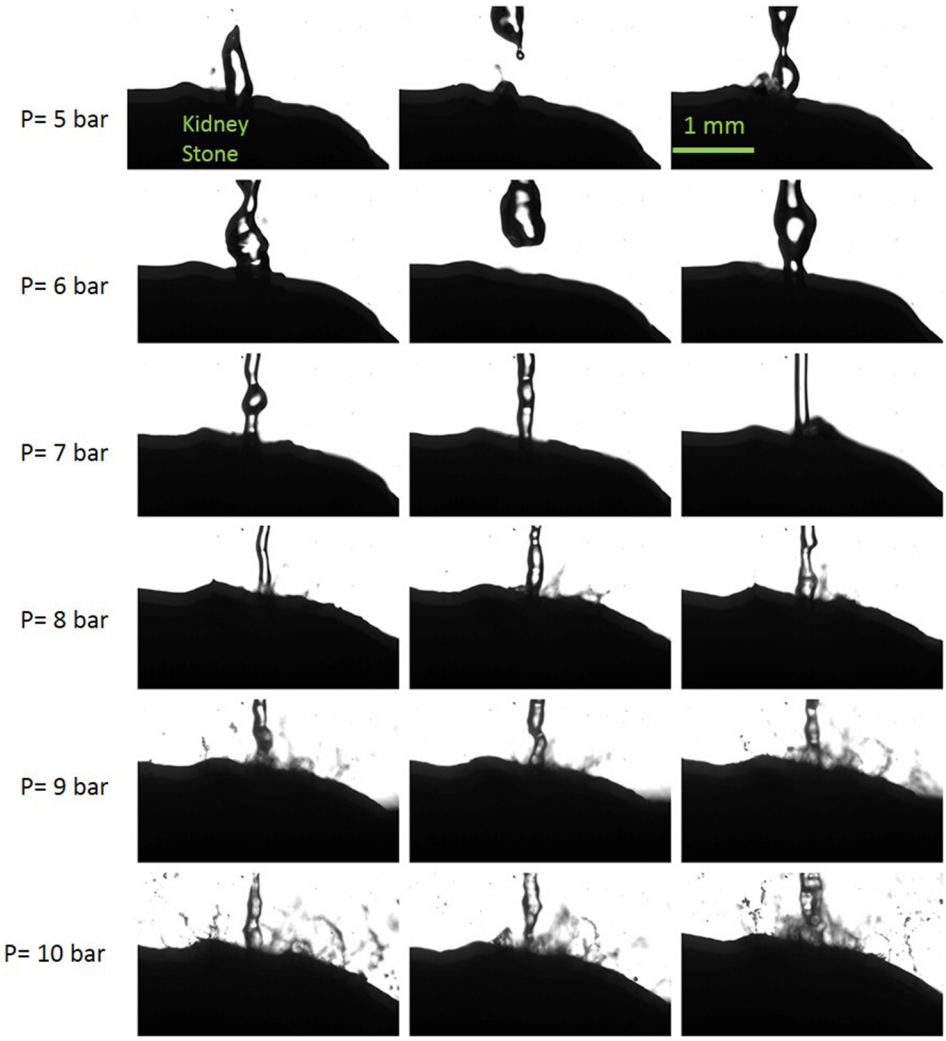


FIG. 4. Interactions between the cavitating flow and urinary stone at upstream pressures within the range of 5–10 bar.

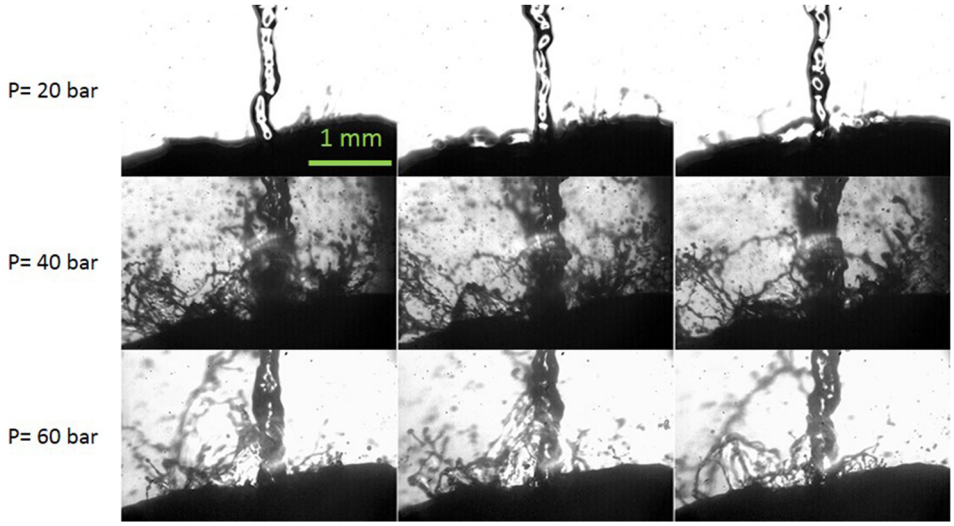


FIG. 5. Interactions between the cavitating flow and urinary stone at upstream pressures within the range of 20–60 bar.

8x to 16x, and the images in Figure 4 were obtained. In these images, the inlet pressure is set to 10 bar and the flow is recorded until the pressure reaches the target value of 10 bar.

The previous studies of the authors were performed for the verification of the hydrodynamic cavitation occurrence inside the microchannel and the investigation of spray characterization under the effect of cavitation phenomenon. They showed that cavitation bubbles moved towards the end of the channel and affected the spray by their collapse inside/outside the microchannel.[17,18,37]

The experiment was repeated for different upstream pressures and interactions between the cavitating flow and urinary stone, and these interactions were visualized and recorded, as shown in Figure 5.

After setting the proper connection between the prototype system with the joystick, experiments were carried out on the urinary stone. Deformations were obtained on the stone at upstream pressures of 5, 10, 20, 40, 60, 80, and 100 bar, using the hydrodynamic cavitation, and the fragmentations were observed using the external high-speed camera and the internal medical camera. The joystick was moved around the stone, and different pressures were applied.

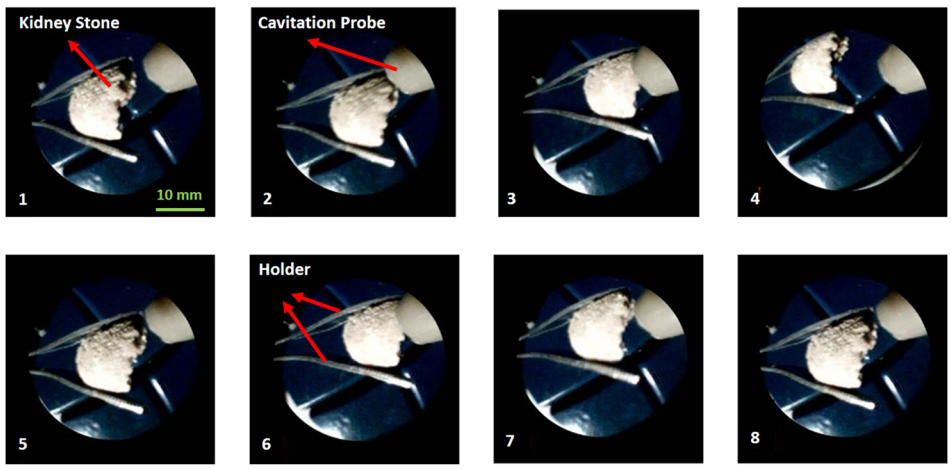


FIG. 6. Depiction of sequential images (with 2 μs time interval) of the urinary stone and cavitation probe captured by a medical camera.

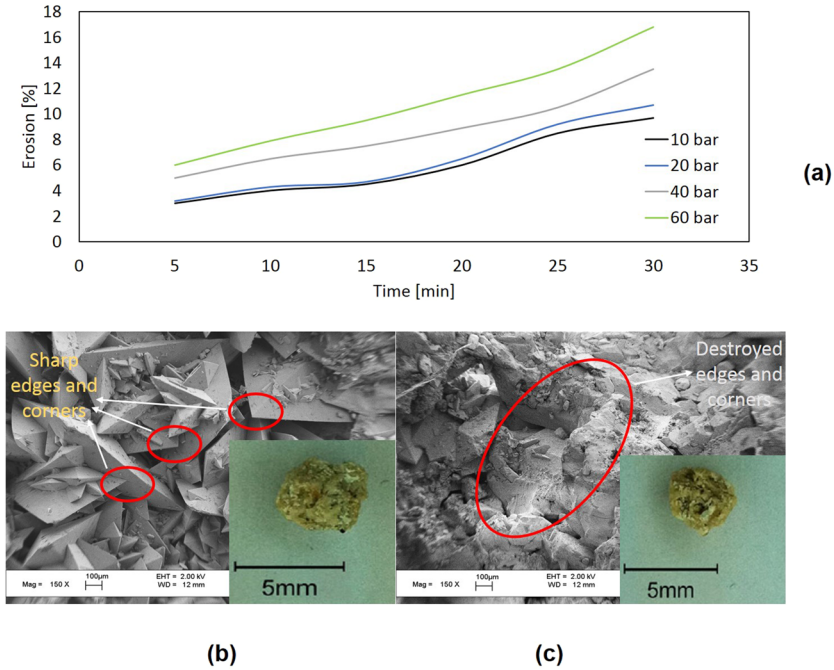


FIG. 7. (a) Erosion (in percentage) relative to the initial mass (~59.1 mg) of the urinary stone with respect to time at the injection pressures of 10, 20, 40 and 60 bar, (b) SEM image of the tested urinary stone before the experiment, and corresponding (c) SEM image of the tested urinary stone after the experiment of injection pressure of 10 bar.

At the final stage of the experiment, the camera and the hydrodynamic cavitation tube were adjusted, and the stone holder was fixed. The flexible tip is circled over different locations on the stone during the exposure of cavitating flow on the urinary stone (Figure 6). The urinary stone was then fixed to a position where the prototype could be reached at an angle, and the position of the cavitation probe was set at the location of the stone using the controller system in the prototype.

Erosion results

The results on the erosion of the urinary stone were collected at different time periods after the exposure to cavitating flow. The erosion ratio was recorded at 5, 10, 15, 20, 25, and 30 minutes, after the exposure of each case to the injection pressure. Figure 7(a) shows the erosion ratio with respect to the time period for the injection pressures of 10, 20, 40 and 60 bar. In these cases, an erosion (in percentage) relative to the initial mass (~59.1 mg) of approximately 10 % and 16 % were obtained after 30 min of cavitating flow exposure on the targeted area on the urinary stone at the upstream pressures of 10 and 60 bar, respectively. Figures 7(b) and 7(c) present SEM images of the tested urinary stone before and after the experiment at the upstream pressure of 10 bar. Well defined edges and corners before the experiments disappear after the experiments.

DISCUSSION

The destructive power of hydrodynamic cavitation was successfully exploited in the fragmentation of the urinary stone. By studying the destructive properties of cavitation, a prototype medical device, which could be used for therapeutic purposes (urinary stone breakage, tissue and tumor ablation, etc.), was developed and presented. The impact of hydrodynamic microscale cavitating flows was assessed by processing the acquired images. With hydrodynamic cavitating flows, a spray was formed at different conical angles extending from the exit of the microprobe, at different upstream pressures. The experiments were performed in vitro on urinary stones, which were surgically removed in Hisar Intercontinental Hospital before experiments, and kept in saline solution at room temperature until experimentation. Hydrodynamic cavitation was successfully exposed on urinary stones,

and a considerable reduction in their sizes was recorded within a short time after the exposure. The presented hydrodynamic cavitation method has some advantages. Ultrasonic-therapy-based systems are might have a high cost, while new generation systems offer reduced cost solutions.[38] This also applies to laser-based and other high-tech medical equipment. The resulting prototype has a potential of offering a cost-effective and energy-efficient solution for kidney stone and benign prostate tissue therapy. Such a prototype has a manufacturing cost lower than lithotripsy devices (lower than $10,000). Thus, the unit price of the resulting hydrodynamic cavitation device is expected to be within the competitive range of other, commercially available products, based on ultrasound therapy. Once the urinary stone is located, the device exposes it to small cavitation bubbles, which break the stone into smaller pieces. Since they have a small size due to the emerging small bubble size, the debris can easily pass through the urinary tract. Ureteroscopy is one of two preferred methods for locating urinary stones in the urinary system. The flexible micromanipulator is equipped with similar type of imaging system used in ureteroscopy. For this purpose, it was made sure that a medical camera (Medigus Ltd, Israel) was integrated to the device and manipulator. Since this camera has a long depth of field (5-50mm for 100° field of view optics), urinary stones can be detected. Thus, an operator can locate and target the urinary stone at the desired spot. Based on the feedback from the images of this camera, the operator can still expose the desired spot to small bubbles with the help of micromanipulator even though the urinary stone moves. It was also shown that a single cavitation probe could cause a significant erosion within 30 minutes (Figs. 6 and 7). The erosion effect could be easily amplified by multiple cavitation probes, which are installed in parallel. Such a configuration could be prepared with standard microfabrication techniques and could also fit to the proposed prototype. In addition, roughness elements on the surfaces of the cavitation probes could be introduced to the system with facile and environmentally friendly surface modification methods so that the intensity of the cavitating flows could be enhanced. As a result, above mentioned urinary stones could be broken into small pieces within a short time of 30 min, which significantly overlaps with the durations in the widely used methods. This prototype also allows in vivo studies. In near future, the authors will test it in in vivo animal studies and clinical studies with the use of multi cavitation probe configurations with modified (roughened) surfaces. Pigs and minipigs will be the most representative alternatives since they have a comparable physiology of the urinary system with humans.

Small scale hydrodynamic cavitation minimizes side effects for tissues and organs around the affected area. As a result, this new approach has potential in attracting the attention of health care professionals and technologists on microfluidics/nanofluidics, thereby opening new avenues in biomedical treatment.

MATERIALS AND METHODS

Micromanipulator fabrication

The parts of the flexible micromanipulator section were designed to have the desired 40° bending angle with the use of the 3D CAD software SolidWorks. The pieces of the first prototype were manufactured by plastic (based on the ProJet 3500 HDMax 3D printer (3D Systems, USA)) to confirm the bending performance. After verification of the design, the pieces were fabricated from steel material. The prototype contains complex parts with dimensions as small as 0.75 mm. Thus, for manufacturing, the M290 (EOS, Germany) 3D direct metal laser sintering (DMLS) method was preferred. An aluminum, profile-based, construction was set up. The fabricated flexible micromanipulator parts, prototype holder, Stewart platform, and tendon guides, were placed on the aluminum-based construction. The Stewart platform was fixed to the base of the aluminum construction. The flexible prototype was attached to the end of the construction. The tips of the tendon wires were fixed at the end of the end-disk, and the other tendon tips were fixed on the Stewart platform by passing through it the tendon guides.

Device characterization

The setup generates cavitating flows with flow restrictive elements, which are microchannels with different diameters. The stainless-steel tubing with a diameter of 4.5 mm was connected to

the micromanipulator containing the cavitation probe and medical camera probe. The connection between the tubes was accomplished with proper Swagelok fittings in order to establish a continuous flow to reach the restrictive element in the cavitation probe, thereby reducing the static pressure. This leads to the generation of cavitation bubbles and cavitating jet flows. Furthermore, the length of the microchannel was adjusted in such a way that the generated bubbles and vapor phase could reach the exit of the channels.

Experimental procedure

The experiments were carried out at different upstream pressures from 5 to 100 bar, while the downstream pressure was fixed at atmospheric pressure. The flow was visualized utilizing a high-speed camera system (in addition to the medical camera) at different segments relative to the exit of the microchannel and injection pressures. The spray structure was captured within a spatial location that spanned the outlet of the channel to the location where the cavitating jet interacted with the urinary stone. The visualization experiments were performed at several upstream pressures ranging from 5 to 100 bar. To study the spray formation, the exposure time was adjusted to a very low value of 1 μs. The images of the cavitating flows were collected by a double-shutter CMOS camera, which allows the acquisition of two successive images with a resolution of 1280×800 pixels^2 (pixel size of 0.02 mm) with a very short time delay between successive frames. The CMOS camera was equipped with a macro camera lens (type K2 DistaMax with focal length, s = 50 mm, and f-number, f = 1.2), and was mounted at a distance of 342 mm from the imaging plane, yielding a magnification of M = 0.137. This optical arrangement ensures that only the central region of the lens is used where aberration can be neglected. The images were exposed to a background illumination mode using a laser shadow probe. This visualization was performed in order to characterize the spray at the outlet of the microchannel in order to use it in the interaction with the urinary stone. Another visualization step was performed with the aid of a medical camera, which was mounted on the micromanipulator parallel to the cavitation probe. In this visualization section, the locations of the targeted area along with the motion of the micromanipulator were characterized for optimizing the fragmentation on the surface of the urinary stone.

Flow characterization

The mass flow rate was obtained by measuring the fluid mass passing from the cross-sectional area of the outlet over a given time period. The experiments were carried out at a broad range of upstream pressures, and all temperature measurements and visualization tests were repeated for several times to ensure the reliability of the obtained results. Using the manufacturer's specification sheets and the propagation characteristics based on the uncertainty propagation method by Kline and McClintock,[39] the average uncertainties in flow rate (±1.4 %), inner diameter (±0.002 mm), and pressure drop (±0.3 %) were obtained.

Ethics approval is not required.

ACKNOWLEDGMENTS

The equipment and characterization support provided by the Sabancı University Nanotechnology Research and Applications Center (SUNUM) is appreciated. This work was supported by TUBITAK (The Scientific and Technological Research Council of Turkey) Support Program for Priority Research Projects Grant, 113S092, Science Academy Outstanding Young Investigator Support Program (BAGEP), Turkish Academy of Science (TUBA) Outstanding Young Investigator Support Program (GEBIP).

The authors declare no competing financial interests.

[1] R. Hofmann, P. Olbert, J. Weber, S. Wille, and Z. Varga, "Clinical experience with a new ultrasonic and lithoclast combination for percutaneous lithoplaxy," BJU International **90**, 16–19 (2002).
[2] A. P. Evan and L. R. Willis, "Extracorporeal shock wave lithotripsy: Complications," *Smith's Textbook on Endourology* (PMPH-USA, Shelton, CT, USA, 2007), pp. 353–365.
[3] N. Vykhodtseva, N. Mcdannold, H. Martin, R. T. Bronson, and K. Hynynen, "Apoptosis in ultrasound-produced threshold lesions in the rabbit brain," Ultrasound Med. Biol. **27**(1), 111–117 (2001).

[4] F. Firestein, L. A. Rozenszajn, L. Shemesh-Darvish, R. Elimelech, J. Radnay, and U. Rosenschein, "Induction of apoptosis by ultrasound application in human malignant lymphoid cells," Ann. New York Acad. Sci. **1010**(1), 163–166 (2003).
[5] P. Wang, A. W. Leung, and C. Xu, "Low-intensity ultrasound-induced cellular destruction and autophagy of nasopharyngeal carcinoma cells," Exp. Therapeutic Med. **2**(5), 849–852 (2011).
[6] X. Wang, Q. Liu, Z. Wang, P. Wang, P. Zhao, X. Zhao, L. Yang, and Y. Li, "Role of autophagy in sonodynamic therapy-induced cytotoxicity in s180 cells," Ultrasound Med. Biol. **36**(11), 1933–1946 (2010).
[7] C. D. Scales, Jr., J. C. Lai, A. W. Dick, J. M. Hanley, J. van Meijgaard, C. M. Setodji, and C. S. Saigal, "Comparative effectiveness of shock wave lithotripsy and ureteroscopy for treating patients with kidney stones," JAMA Surg. **149**(7), 648–653 (2014).
[8] A. E. Krambeck, N. L. Miller, M. R. Humphreys, S. Y. Nakada, J. D. Denstedt, H. Razvi *et al.*, "Randomized controlled, multicentre clinical trial comparing a dual-probe ultrasonic lithotrite with a single-probe lithotrite for percutaneous nephrolithotomy," BJU International **107**, 824–828 (2010).
[9] S. C. Kim, B. R. Matlaga, W. W. Tinmouth, R. L. Kuo, A. P. Evan, J. A. McAteer, J. C. Williams, and J. E. Lingeman, Jr., "In vitro assessment of a novel dual probe ultrasonic intracorporeal lithotriptor," J. Urology **177**(4), 1363–1365 (2007).
[10] M. Atar, M. N. Bodakci, A. A. Sancaktutar, N. Penbegul, H. Soylemez, Y. Bozkurt, N. K. Hatipoglu, and S. Cakmakci, "Comparison of pneumatic and laser lithotripsy in the treatment of pediatric ureteral stones," J. Pediatric Urology **9**, 308–312 (2013).
[11] R. Hofmann, P. Olbert, J. Weber, S. Wille, and Z. Varga, "Clinical experience with a new ultrasonic and lithoclast combination for percutaneous lithoplaxy," BJU International **90**, 16–19 (2002).
[12] A. Diri, B. Resorlu, M. Astarci, A. Unsal, and C. Germiyonoglu, "Tissue effects of intracorporeal lithotripsy techniques during percutaneous nephrolithotomy: Comparison of pneumatic and ultrasonic lithotripters on rat bladder," Urological Res. **40**, 409–413 (2012).
[13] H. A. Razvi, J. D. Denstedt, S. S. Chun, and J. L. Sales, "Intracorporeal lithotripsy with the holmium:YAG laser," J. Urology **156**, 912–914 (1996).
[14] V. Tugcu, F. E. Su, N. Kalfazade, S. Sahin, B. Ozbay, and A. I. Tasci, "Percutaneous nephrolithotomy (PCNL) in patients with previous open stone surgery," Int. Urol. Nephrol. **40**(4), 881–884 (2008).
[15] A. K. Hemal and R. Kumar, "Retrograde intrarenal surgery," Indian J. Urology **16**(2), 83–87 (2000).
[16] J. L. Huffman, D. H. Bagley, and E. S. Lyon, "Extending cystoscopic techniques into the ureter and renal pelvis, experience with ureteroscopy and pyeloscopy," The JAMA Network (1983).
[17] M. Ghorbani, A. Khalili Sadaghiani, M. Yildiz, and A. Kosar, "Experimental and numerical investigations on the spray collapse under the effect of cavitation phenomenon in a microchannel," J Mech Sci Techn. **31**(1), 235–247 (2017).
[18] M. Ghorbani, M. Yildiz, D. Gozuacik, and A. Kosar, "Cavitating nozzle flow in micro and mini channels under the effect of turbulence," J Mech Sci Techn. **30**(6), 2565–2581 (2016).
[19] E. Yilmaz, A. Haciislamoglu, U. Kisa, O. Dogan, E. Yuvanc, and E. Batislam, "Ways in which SWL affects oxidant/antioxidant balance," Urolithiasis **41**(2), 137–141 (2013).
[20] M. Ghorbani, O. Oral, S. Ekici, D. Gozuacik, and A. Kosar, "Review on lithotripsy and cavitation in urinary stone therapy," IEEE Reviews in Biomedical Engineering **9**, 264–283 (2016).
[21] J. Shang, C. J. Payne, J. Clark, D. P. Noonan, K.-W. Kwok, A. Darzi, and G.-Z. Yang, "Design of a multitasking robotic platform with flexible arms and articulated head for minimally invasive surgery," Europe PMC Funders Group, 1988–1993, 2012.
[22] P. Giataganas, N. Evangeliou, Y. Koveos, E. Kelasidi, and A. Tzes, "Design and experimental evaluation of an innovative SMA-based tendon-driven redundant endoscopic robotic surgical tool," 19th Mediterranean Conference on Control and Automation Aquis Corfu Holiday Palace, Corfu, Greece, June 20-23, 2011.
[23] R. J. Hendrick, S. D. Herrell, and R. J. Webster III, "A multi-arm hand-held robotic system for transurethral laser prostate surgery," 2014 IEEE International Conference on Robotics & Automation (ICRA) Hong Kong Convention and Exhibition Center, May 31-June 7, 2014, Hong Kong, China.
[24] G. M. Flanningan, J. S. K. Gelister, J. G. Noble, and E. J. G. Milroy, "Rigid versus flexible cystoscopy a controlled trial of patient tolerance," BJU International **62**(6), 537–540 (1988).
[25] S. W. Denholm, I. G. Conn, J. E. Newsam, and G. D. Chisholm, "Morbidity following cystoscopy: Comparison of flexible and rigid techniques," BJU International **66**(2), 152–154 (1990).
[26] M. R. Erdem, K. Topaloğlu, O. E. Yücebaş, F. Şengör, A. R. Aslan, C. Tosun, M. A. Ramazanoğlu, and S. Duvar, "Better comfort for both patient and doctor: Prospective randomized study about flexible and rigid cystoscopy," J. Urological Surgery **2**, 65–68 (2015).
[27] Z. Li and R. Du, "Design and analysis of a bio-inspired wire-driven multi-section flexible robot," Int. J. Advanced Robotic Sys. **10**, 4 (2013).
[28] Z. Li, J. Feiling, H. Ren, and H. Yu, "A novel tele-operated flexible robot targeted for minimally invasive robotic surgery," Engineering **1**(1), 73–78 (2015).
[29] J. Estevadeordal and L. Goss, "PIV with LED: Particle shadow velocimetry (PSV)," in 43rd AIAA aerospace sciences meeting and exhibit, meeting papers, 12355–12364, 2005.
[30] F. Durst, A. Melling, and J. H. Whitelaw, "Principles and practice of laser-Doppler anemometry," NASA STI/Recon Technical Report A **76**, 47019 (1976).
[31] R. Ray, P. Henshaw, N. Biswas, and C. Sak, "Evaporation of water spray from a rotary bell atomizer using a phase Doppler anemometer," Atomization Sprays **25**, 7 (2015).
[32] Q. Fu and W. Sun, "Mie theory for light scattering by a spherical particle in an absorbing medium," Applied Optics **40**(9), 1354–1361 (2001).
[33] R. C. Gonzalez, *Digital Image Processing* (Pearson Education, India, 2009).

[34] G. Alcan, M. Ghorbani, A. Kosar, and M. Unel, "Vision based cone angle estimation of bubbly cavitating flow and analysis of scattered bubbles using micro imaging techniques," IEEE 41st Annual Conference of the Industrial Electronics Society, 003473–003474, 2015.
[35] M. Ghorbani, G. Alcan, M. Unel, D. Gozuacik, S. Ekici, H. Uvet, A. Sabanovic, and A. Kosar, "Visualization of microscale cavitating flow regimes via particle shadow sizing imaging and vision based estimation of the cone angle," Exp. Therm. Fluid Sci. **78**, 322–333 (2016).
[36] G. Alcan, M. Ghorbani, A. Kosar, and M. Unel, "A new visual tracking method for the analysis and characterization of jet flow," Flow Measure. Instrumentation **51**, 55–67 (2016).
[37] M. Ghorbani, G. Alcan, A. Mohammadi, A. Khalili Sadaghiani, M. Unel, D. Gozuacik, and A. Kosar, "Characterization and pressure drop correlation for sprays under the effect of micro scale cavitation," Exp. Therm. Fluid. Sci. **91**, 89–102 (2018).
[38] T. Ikeda, S. Yoshizawa, M. Tosaki, J. S. Allen, S. Takagi, N. Ohta, T. Kitamura, and Y. Matsumoto, "Cloud cavitation control for lithotripsy using high intensity focused ultrasound," Ultrasound Med Biol. **32**(9), 1383–1397 (2006).
[39] S. J. Kline and F. McClintock, "Describing uncertainties in single-sample experiments," Mech. Eng. **75**(1), 3–8 (1953).